



# A New Stellar Mass Proxy for Subhalo Abundance Matching

CHEN-YU CHUANG <sup>1,2</sup> AND YEN-TING LIN <sup>2</sup>

<sup>1</sup>*Institute of Astronomy, National Tsing Hua University, Hsinchu 30013, Taiwan*

<sup>2</sup>*Institute of Astronomy and Astrophysics, Academia Sinica, Taipei 10617, Taiwan*

Submitted to AAS Journals

## ABSTRACT

Subhalo abundance matching (SHAM) has played an important role in improving our understanding of how galaxies populate their host dark matter halos. In essence, the SHAM framework is to find a dark matter halo property that best correlates with an attribute of galaxies, such as stellar mass. The peak value of the maximum circular velocity ( $V_{\text{max}}$ ) a halo/subhalo has ever attained throughout its lifetime,  $V_{\text{peak}}$ , has been a popular choice for SHAM. A recent study by [Tonnesen & Ostriker \(2021\)](#) suggested that quantity  $\phi$ , which combines the present-day  $V_{\text{max}}$  and the peak value of halo dark matter mass, performs better in predicting stellar mass than  $V_{\text{peak}}$ . Inspired by their approach, in this work, we find that further improvement can be achieved by a quantity  $\psi_5$  that combines the 90th percentile of  $V_{\text{max}}$  a halo/subhalo has ever achieved with the 60th percentile of the dark matter halo time variation rate. Tests based on the simulation *IllustrisTNG300* show that our new SHAM scheme, with just three free parameters, can improve the stellar mass prediction and mass-dependent clustering by 15% and 16% from  $\phi$ , respectively, over the redshift range  $z = 0 - 2$ .

**Keywords:** Galaxy formation (595) — Galaxy physics (612) — Galaxy dark matter halos (1880)

## 1. INTRODUCTION

Among the methods employed to study the galaxy–halo connection (in simplest terms, how galaxies populate dark matter halos; see [Wechsler & Tinker 2018](#) for a recent review), subhalo abundance matching (SHAM; see e.g., [Kravtsov et al. 2004](#); [Vale & Ostriker 2004](#); [Tasitsiomi et al. 2004](#); [Conroy et al. 2006](#); to name only a few early works) is popular for its simplicity – typically only involving a couple of free parameters, the model galaxies produced by the method by construction match the observed galaxy stellar mass (or luminosity) function, as well as the stellar (or luminosity) dependence of the two-point correlation function (2PCF).

In the SHAM framework, one essentially is seeking a dark matter halo property  $X$  that is most tightly correlated with a galaxy property (typically the stellar mass,  $M_*$ ). It has been a popular choice to set  $X = V_{\text{peak}}$ , the peak value of the maximum circular velocity ( $V_{\text{max}}$ ) a halo (or subhalo) has ever attained. With the inclusion of some scatter  $\sigma_V$  between  $V_{\text{peak}}$  and  $M_*$ , the model is shown to be able to best reproduce the observed 2PCFs of galaxies selected above different stellar mass thresholds, compared to models that use other properties as

$X$ , such as peak (sub)halo mass throughout its lifetime ( $M_{\text{DM,peak}}$ ; e.g., [Reddick et al. 2013](#); [Zentner et al. 2014](#); but see [Masaki et al. 2022](#)).

[Lehmann et al. \(2017\)](#) were among the first to consider  $X$  to be a combination of multiple halo properties. Recently, [Tonnesen & Ostriker \(2021, hereafter TO21\)](#) proposed a new property,  $X = \phi \equiv V_{\text{max},0}/v_{\text{max},0@12.7} + M_{\text{DM,peak}}/(10^{12.7}M_\odot)$  (please refer to equation 7 below for the definition of these terms), which is shown to be an excellent stellar mass proxy. Inspired by their approach, here we explore variants to  $\phi$ , and propose a new property  $\psi_5$  that further improves the accuracy in stellar mass prediction by 15% with respect to that of  $\phi$ .

This paper is structured as follows. In Section 2 we describe the simulation and the loss metrics used for our abundance matching (AM) scheme. Then in Section 3 we present our methodology for finding the best stellar mass indicator, which is referred to as  $\psi_5$ . Our results are presented in Section 4, where we show the performance of  $\psi_5$ , in terms of reproducing the stellar mass and color dependencies of galaxy clustering for mock galaxies from *IllustrisTNG300* ([Pillepich et al.](#)

2018; Springel et al. 2018, hereafter TNG300) from  $z = 0$  to  $z = 2$ . We discuss and summarize our results in Section 5 and Section 6, respectively.

## 2. SIMULATION AND METHODS

We test alternatives to  $\phi$  using the TNG300 simulation suites, and quantify the performance by the prediction of  $M_\star$  and stellar mass/color-dependent 2PCF. In this section, we first describe how we select galaxies from the simulation, then explain how the 2PCF is measured, as well as how the performance of the variants of  $\phi$  (which shall be referred to as  $\psi$ ) is evaluated.

### 2.1. TNG300

We extract the dark matter and baryonic features from TNG300, which has a box of 300 Mpc on a side and contains  $(2500)^3$  dark matter particles and gas particles. To select the well resolved galaxies, we choose model galaxies with stellar mass<sup>1</sup>  $M_\star \geq 10^9 h^{-1} M_\odot$  and the dark matter subhalos with dark matter mass  $M_{DM} \geq 10^{11} h^{-1} M_\odot$  in the dark matter only (DMO) counterpart of TNG300. Then, we separate the galaxies into satellites and centrals using the subhalo catalog of TNG300.

Following TO21, we abundance match the stellar mass for the “all”, “central”, and “satellite” groups of galaxies, while a combined sample in which “central”, “satellite” are fit separately is labeled as the “mixed” group. To reproduce the color dependence of the 2PCFs (see Section 2.2, we also separate the subhalos into blue and red samples by the color of the galaxies they host:

$$(u - g)_{\text{cut}} = -0.031M_g - 0.065z + 0.695 \quad (1)$$

where the  $u - g$  is the SDSS  $u - g$  color,  $M_g$  is the  $g$ -band absolute magnitude, and  $z$  is the redshift (following Skibba et al. 2014). We obtain the magnitudes of subhalos from the catalog published by Nelson et al. (2018).

### 2.2. 2PCF

A 2PCF,  $\xi(r)$ , is a measure of excess probability of finding a pair of galaxies separated by a distance  $r$  over a random distribution. Observationally, to avoid contamination from peculiar velocities along the line of sight (LOS), one typically integrates along the redshift dimension and obtain the projected 2PCF, defined as

$$w_p(r_p) = \int_{-\infty}^{\infty} \xi(r_p, \pi) d\pi \approx 2 \times \int_0^{\pi_{\text{max}}} \xi(r_p, \pi) d\pi \quad (2)$$

<sup>1</sup> From the SubhaloMassType field in the TNG300 catalog.

where  $r_p$  is the separation on the plane-of-the sky and  $\pi$  is the distance along the LOS. The upper limit of LOS integration,  $\pi_{\text{max}}$ , is chosen to be 40 Mpc, which is consistent with the choice of actual measurements done with real data (e.g., Lin et al. 2016, 2022).

In Sections 4.2 & 4.3, we compare the 2PCFs from the true galaxy position and that from the abundance matched galaxy position in different  $M_\star$  and color bins. We make use of a high-performance package, **Corrfunc** (Sinha & Garrison 2020; Sinha & Garrison 2019), to calculate the  $w_p$ ’s.

### 2.3. Loss Measures

The primary objective of our study is to predict the  $M_\star$  of each subhalo accurately while reproducing  $w_p$  in the simulation. To measure the difference between the prediction and the ground truth, we define three metrics. We use the scatter to gauge the  $M_\star$  predictions:

$$\sigma = \sqrt{\frac{1}{N} \sum_i^N (\Delta y_i - \overline{\Delta y})^2} \quad (3)$$

where  $N$  is the total number of galaxies,  $\Delta y_i = \log(M_{\star,i}) - \log \widehat{M}_{\star,i}$  is the residual of single  $M_\star$  prediction and  $\overline{\Delta y}$  is the average of the residual. To compare our results with TO21, we also calculate the error, defined as

$$\text{Error} = \frac{\sum_i^N |\log(M_{\star,i}/\widehat{M}_{\star,i})|}{N} \quad (4)$$

For  $w_p$  predictions, we obtain the average of the fractional error for the  $r_p$  and  $M_\star$  bins.

$$L = \frac{1}{N_{M_\star} \times N_{r_p}} \sum_{N_{M_\star}} \sum_{N_{r_p}} \left| \frac{w_p(r_p, M_\star) - \widehat{w}_p(r_p, M_\star)}{w_p(r_p, M_\star)} \right| \quad (5)$$

where  $N_{M_\star}$  and  $N_{r_p}$  are the numbers of  $M_\star$  bins and  $r_p$  bins, respectively. The uncertainty is measured by jackknife resampling. We calculate the  $w_p$  with each jackknife sample and obtain the uncertainty via

$$\sigma_w(w_p) = \sqrt{\frac{N-1}{N} \sum_j^N (w_p - \widehat{w}_{p,j})^2} \quad (6)$$

where  $N = 27$  is the number of jackknife samples, and  $\widehat{w}_{p,j}$  is the projected 2PCF associated with given jackknife sample. Here we do not include scatter in our  $w_p$  estimation.

## 3. RANK ORDERING SCHEMES

The simplest SHAM scheme is assuming a one-to-one correspondence between galaxies and dark matter

(sub)halos of the same number density, where the rank ordering is through  $M_*$  for galaxies, and dark matter mass for (sub)halos. However, the dark matter mass of subhalos usually suffers from tidal stripping, and thus is not able to adequately reflect the rank order of stellar mass. TO21 improved this by introducing two parameters, the  $V_{\max}$  at  $z = 0$  ( $V_{\max,0}$ ) and  $M_{\text{DM,peak}}$ . These properties are shown to be less sensitive to tidal stripping than dark matter mass. By combining these parameters into a single dimensionless parameter

$$\phi = V_{\max,0}/V_{\max,0@12.95} + M_{\text{DM,peak}}/10^{12.95} M_{\odot} \quad (7)$$

(a “pivot mass” of  $M_{\text{DM,peak}} = 10^{12.95} M_{\odot}$  is introduced to normalize  $\phi$ ;  $V_{\max,0@12.95}$  is  $V_{\max,0}$  for a halo of the pivot mass.<sup>2</sup>), TO21 achieved an improvement of 27% compared to using dark matter mass alone for the  $M_*$  prediction.<sup>3</sup> In our work, we try to compare  $\phi$  with the  $X$  we developed with TNG300. Thus, we refit the pivot mass for  $\phi$  in the simulation and find  $M_{\text{DM,peak}} = 10^{12.95} M_{\odot}$  for redshift 0.

Our goal is to seek other parameter combinations  $\psi$  that performs better than  $\phi$ , particularly for the clustering properties, an aspect not addressed fully in TO21. Although the maxima of subhalo properties throughout their lifetimes such as  $V_{\text{peak}}$  and  $M_{\text{DM,peak}}$  are shown to better trace  $M_*$ , the stochastic nature of those features as seen from the simulations can cause additional scatter. Thus, instead of using the maximum (i.e., 100th percentile) of those properties, we use a specific percentile for those properties to avoid the scatter due to stochasticity. We have tried the 10th, 20th, ... 100th (= peak) percentile for  $V_{\max}$  and  $M_{\text{DM}}$  throughout the lifetimes of subhalos, and conduct abundance matching using different percentiles of each properties. It is found that the 90th percentile can predict  $M_*$  with the smallest scatter among all cases considered for  $V_{\max}$  and  $M_{\text{DM}}$  (here after  $V_{\max,90\%}$  and  $M_{\text{DM,90\%}}$ ).<sup>4</sup> Replacing the properties in  $\phi$  with the percentiled properties, we have found that the scatter of abundance matching decreases by  $\sim 12.5\%$ .

Motivated by the finding that the peak value of the quantities often used in SHAM does not always lead to the best results, we then conduct a thorough examination for the performance of *all* the dark matter subhalo

properties provided by TNG300 of different percentiles. The best alternatives of  $V_{\max,90\%}$  is  $V_{\text{disp},80\%}$  while those of  $M_{\text{DM,90\%}}$  are  $M_{R_{\max},80\%}$  and  $|\dot{M}_{\text{DM}}|_{60\%}$ , where  $V_{\text{disp}}$  is the velocity dispersion of a subhalo,  $M_{R_{\max}}$  is the dark matter mass within the radius that corresponds to  $V_{\max}$ , and  $|\dot{M}_{\text{DM}}|$  is the absolute subhalo dark matter mass variation rate. We will show in Section 4 that  $X$  based on the combinations of these quantities can improve the prediction of stellar mass and  $w_p$ , and define six candidates for  $X$  as:

$$\psi_1 = \frac{V_{\max,90\%}}{V_{\max,90\%@13.3}} + \frac{M_{\text{DM,90\%}}}{M_{\text{DM,90\%@13.3}}} \quad (8)$$

$$\psi_2 = \frac{V_{\text{disp},80\%}}{V_{\text{disp},80\%@13.6}} + \frac{M_{\text{DM,90\%}}}{M_{\text{DM,90\%@13.6}}} \quad (9)$$

$$\psi_3 = \frac{V_{\max,90\%}}{V_{\max,90\%@13.5}} + \frac{M_{R_{\max},80\%}}{M_{R_{\max},80\%@13.5}} \quad (10)$$

$$\psi_4 = \frac{V_{\text{disp},80\%}}{V_{\text{disp},80\%@13.8}} + \frac{M_{R_{\max},80\%}}{M_{R_{\max},80\%@13.8}} \quad (11)$$

$$\psi_5 = \frac{V_{\max,90\%}}{V_{\max,90\%@13.2}} + \frac{|\dot{M}_{\text{DM}}|_{60\%}}{|\dot{M}_{\text{DM}}|_{60\%@13.2}} \quad (12)$$

$$\psi_6 = \frac{V_{\text{disp},80\%}}{V_{\text{disp},80\%@13.7}} + \frac{|\dot{M}_{\text{DM}}|_{60\%}}{|\dot{M}_{\text{DM}}|_{60\%@13.7}} \quad (13)$$

where the parameters with a subscript @ are the normalization factor at a fitted pivot  $M_{\text{DM,peak}}$  right after. We tried a range of pivot masses ( $M_{\text{DM,peak}} = 10^{10.0} - 10^{14.0} M_{\odot}$ ) and select the one which minimizes the scatter of  $M_*$  prediction for each  $\psi$ 's. The subhalo properties along the main primary branch are used to calculate  $\dot{M}_{\text{DM}}$  and all the parameters with the subscript of “peak” or a certain percentile.

## 4. RESULTS

### 4.1. Stellar Mass Prediction

We show in Table 1 the performance of each AM scheme in stellar mass prediction. In the upper-left part in each redshifts of the table, the lifetime peak properties are improved by selecting an optimized percentile for all four groups of galaxies mentioned in Section 2.1. In the lower-left part of each redshift, all  $\psi$ 's show relatively better  $M_*$  prediction to the original  $\phi$  for the four groups. It is also shown that  $\psi_1$  performs slightly worse than the other  $\psi$ 's, which means a better prediction of  $M_*$  can be achieved by replacing  $V_{\max,90\%}$  and  $M_{\text{DM,90\%}}$  with different properties.

In Figure 1, we compare the prediction errors with respect to true  $M_*$  using different AM schemes. The contours show the density distribution of the data points in

<sup>2</sup> The mass is the sum of gravitationally bounded particles as provided by the SUBFIND algorithm (Springel et al. 2001)

<sup>3</sup> As TO21 worked on IllustrisTNG100 (with a box size of  $100^3 \text{ Mpc}^3$ ), we have to re-fit the pivot mass. Using their original pivot mass ( $M_{\text{DM,peak}} = 10^{12.7} M_{\odot}$ ), the improvement is 34% (TO21).

<sup>4</sup> With such a notation,  $V_{\text{peak}} \equiv V_{\max,100\%}$ .

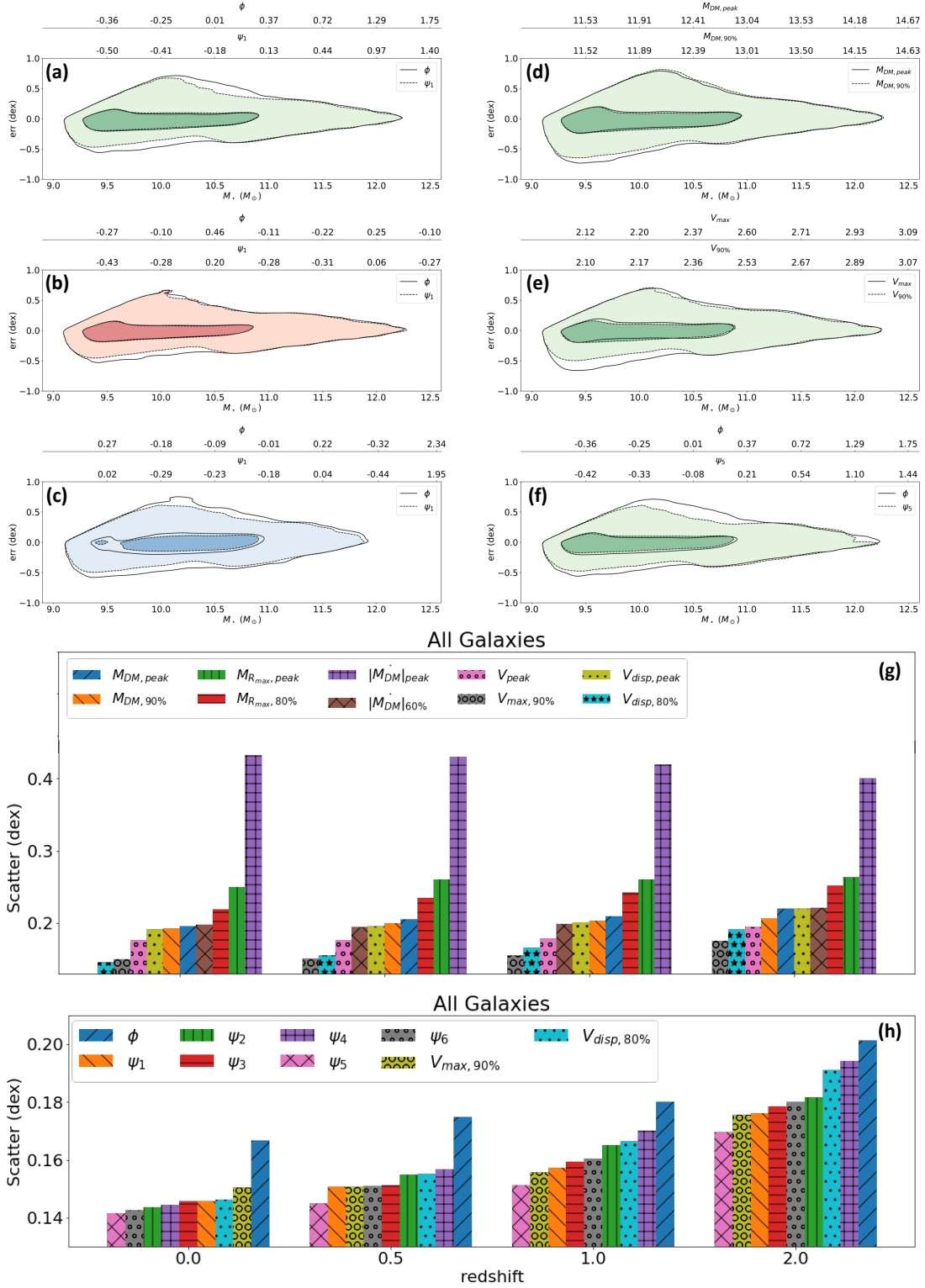


**Figure 1.** Panels (a) to (e): The error of the stellar mass prediction corresponding to stellar mass using the AM scheme of  $\phi$  and  $\psi_1$  for panels (a) to (c),  $M_{DM,peak}$  and  $M_{DM,90\%}$  for panel (d),  $V_{peak}$  and  $V_{max,90\%}$  for panel (e), and  $\phi$  and  $\psi_5$  for panel (f). The green, red, and blue contours represent the predictions of “all”, “central” and “satellit” groups, respectively. There are two contour lines for each AM scheme, which denote the data point density of 0.05 and 0.5 (normalized to maxima of 1). Panels (g) and (h): The overall scatter at several redshifts with different AM scheme denoted on the top left of the panel. The bars for each redshift bin are sorted so that the AM scheme with lowest scatter is on the left.

the panels. A well performed AM scheme should have the contours closer to the horizontal line at zero error. Panel (a) of the Figure shows that the main improvement from  $\phi$  to  $\psi_1$  is for  $\log(M_*/M_\odot) < 11.0$ . Panels (b) and (c) show that the improvement in central galaxies is limited to lower mass galaxies, while that of the satellites also occurs in higher mass galaxies as well. Panels (d) and (e) show the AM performances of individual parameters. Here, we can see that the improvement from  $M_{\text{peak}}$  to  $M_{\text{DM},90\%}$  is lower than that of  $V_{\text{peak}}$  to  $V_{\text{max},90\%}$ . Panel (f) shows the error distribution of  $\psi_5$ , which has the best performance among all AM schemes considered here. Finally, panels (g) and (h) show the scatter of all AM schemes at several different redshifts. We can see that the scatters of all the  $\psi$ 's are smaller than that of  $\phi$  at all redshifts.

#### 4.2. Stellar Mass Dependence of Projected Two-Point Correlation Function

In Table 1, the upper-right part in each redshift of the table shows that the peak properties has larger error for projected 2PCF prediction than the percentile properties, except for the  $M_{\text{DM}}$  properties. In the lower-right of each redshift, we can also find out that the  $\psi$ 's predictions of  $w_p$  are better than that of  $\phi$ . Figure 2 shows the ratio of the predicted  $w_p$  over true  $w_p$ . The first row (panels a to c) and the second row (panels d to f) compare the performances between the peak valued quantities to the percentiled quantities and that between  $\phi$  to  $\psi$ 's, respectively. We see that the major difference of  $w_p$  ratio comes in the lowest and highest  $M_*$  bins while the difference in the middle  $M_*$  bin is not obvious. Panels (g) and (h) show that while  $\psi_5$  results in the best  $w_p$  prediction at  $z = 0$ , while the  $|\dot{M}_{\text{DM}}|_{60\%}$  outperforms  $\psi_5$  at all the other redshifts by a small margin.

#### 4.3. Stellar Mass and Color Dependence of Projected Two-Point Correlation Function

The upper right part in each redshift of Table 1 shows the error of  $w_p$  predictions for the red and blue galaxies. For  $M_{\text{DM}}$ ,  $M_{\text{Rmax}}$  and  $\dot{M}_{\text{DM}}$ , replacing the peak values with percentiled quantities worsens the  $w_p$  predictions for the red galaxies, while improves the predictions for the blue ones. On the other hand, for  $V_{\text{max}}$  and  $V_{\text{disp}}$ , the replacement of peak values with percentiled quantities improves the  $w_p$  predictions for both blue and red galaxies. In the bottom right in each redshift, the  $\psi$ 's outperforms  $\phi$  in both types of galaxies.

Figure 3 and Figure 4 show the same quantities as Figure 2, but for red and blue galaxies, respectively. Same as on Figure 2, the major difference of  $w_p$  occurs at the lowest and highest  $M_*$  bins for both blue and red

galaxies. For the  $w_p$  prediction of red galaxies,  $M_{\text{DM},\text{peak}}$  performs better than  $M_{\text{DM},90\%}$  in all  $M_*$  bins while  $V_{\text{peak}}$  performs roughly the same as  $V_{\text{max},90\%}$ . In the middle  $M_*$  bin,  $\phi$  performs better than  $\psi_1$ , while  $\psi_5$  performs better than  $\phi$ . For most of the redshifts,  $\psi_5$  is the best in predicting  $w_p$  for red galaxies. For the  $w_p$  prediction of blue galaxies,  $M_{\text{DM},90\%}$  and  $V_{\text{max},90\%}$  performs better than  $V_{\text{peak}}$  and  $M_{\text{DM},\text{peak}}$  in the lower two  $M_*$  bins. The performance of all properties in the highest  $M_*$  bins does not show much variation due to the small number of galaxy pairs. For most of the redshifts,  $|\dot{M}_{\text{DM}}|_{60\%}$  is the best for  $w_p$  prediction of blue galaxies, outperforming  $\psi_5$  with a small margin. Overall speaking,  $\psi_5$  is still reliable for reproducing color-dependent clustering.

## 5. DISCUSSION

Using the halos and mock galaxies from TNG300, we have shown that our best stellar mass proxy,  $\psi_5$ , performs better compared to both the popular choice of  $V_{\text{peak}}$ , as well as the parameter  $\phi$  proposed by TO21, in terms of predicting the stellar mass. Furthermore, when used in SHAM,  $\psi_5$  can reliably reproduce both the stellar mass and color dependencies of the 2PCFs at  $z = 0 - 2$  better than  $V_{\text{peak}}$ . Whereas the usual implementation of  $V_{\text{peak}}$  model has one free parameter (the scatter between  $V_{\text{peak}}$  and  $M_*$ ; see below), our  $\psi_5$  model has three (the percentiles for  $V_{\text{max}}$  and  $|\dot{M}_{\text{DM}}|$ , and the normalizing halo mass). Nonetheless, the better performances in  $M_*$  prediction (and hence the stellar mass dependence of  $w_p$ ) should outweigh the extra degrees of freedom.

In Section 3, we argued that the success of our method is attributed to the use of percentiled quantities, which effectively smooths the stochastic behaviour of dark matter subhalo properties. Here we provide a more quantitative analysis on the evolution of  $M_{\text{DM}}$ ,  $M_{\text{Rmax}}$ ,  $|\dot{M}_{\text{DM}}|$ ,  $V_{\text{max}}$  and  $V_{\text{disp}}$  for the subhalos. For each quantity mentioned above, we first obtain the moving average with a window size of 10 snapshots along the time axis for each subhalo, and subtract the original values with averaged values to obtain the residual of property history. Next, we perform a Fast Fourier Transform (FFT) to the residual to obtain an amplitude and frequency relation. Lastly, we calculate the average frequency for each subhalo weighted by the amplitude. We define this value as the stochasticity of a subhalo for a certain dark matter property. Now, we can compare the average stochasticity ( $S$ ,  $\text{Gyr}^{-1}$ ) of the properties with the relative improvement from the chosen percentiled quantities instead of the peak values for each properties. In Table 1, the relative improvement of scatter in the ‘‘All’’ group for each property can be obtained



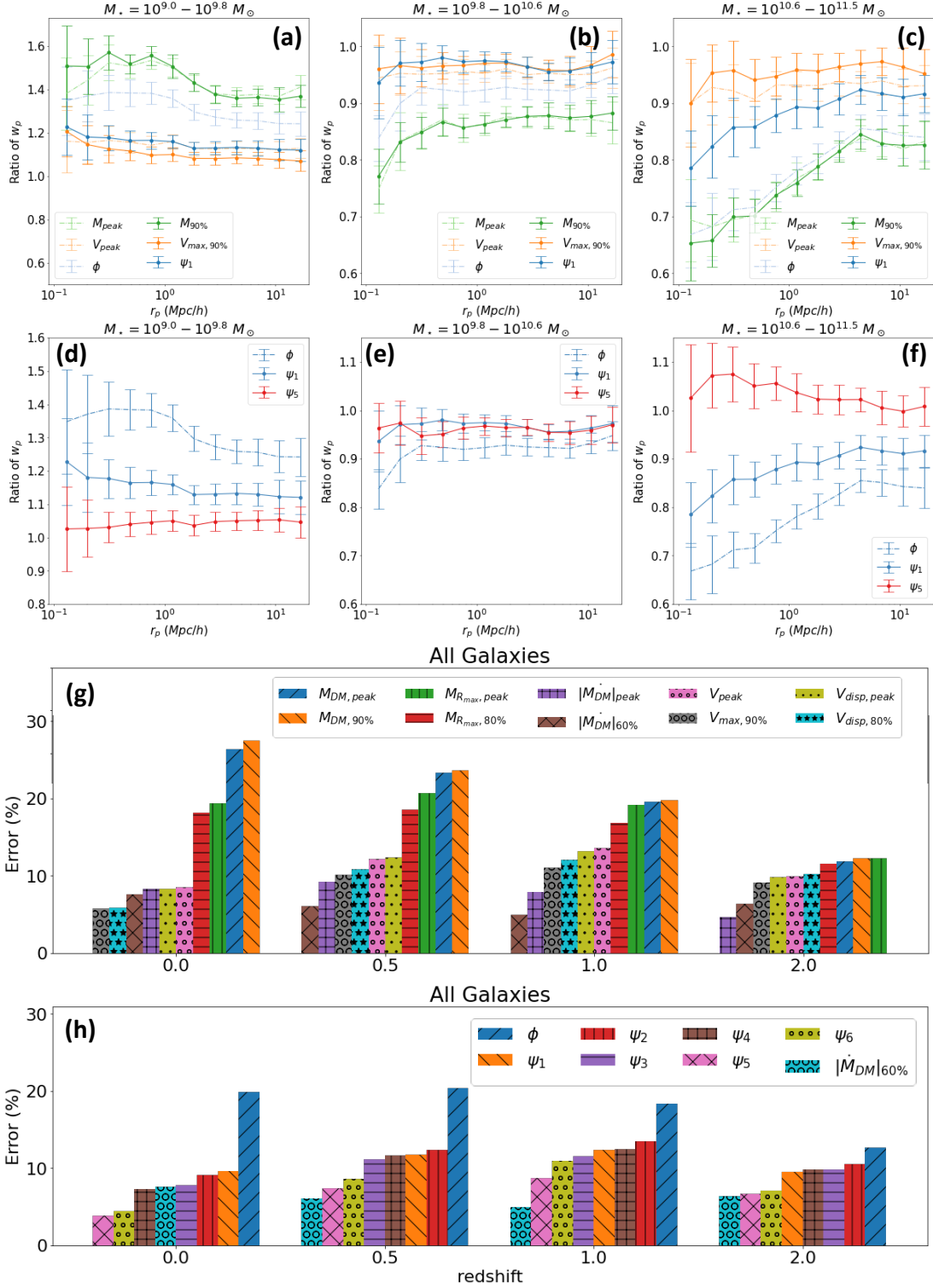


**Figure 2.** Panels (a) to (f): The data points denote the rational difference in projected two point correlation function between true and abundance matched galaxy distribution while the error bars are the Jackknife uncertainties. The mass range of each stellar mass bin is denoted on top of each panel. (g) and (f) show the fractional difference of the clustering averaged over all  $r_p$  bins and  $M_*$  bins in the “all” group. The bar at each redshift is sorted the same way as Figure 1. The data points with Jackknife uncertainties larger than 0.2 are omitted in all panels.

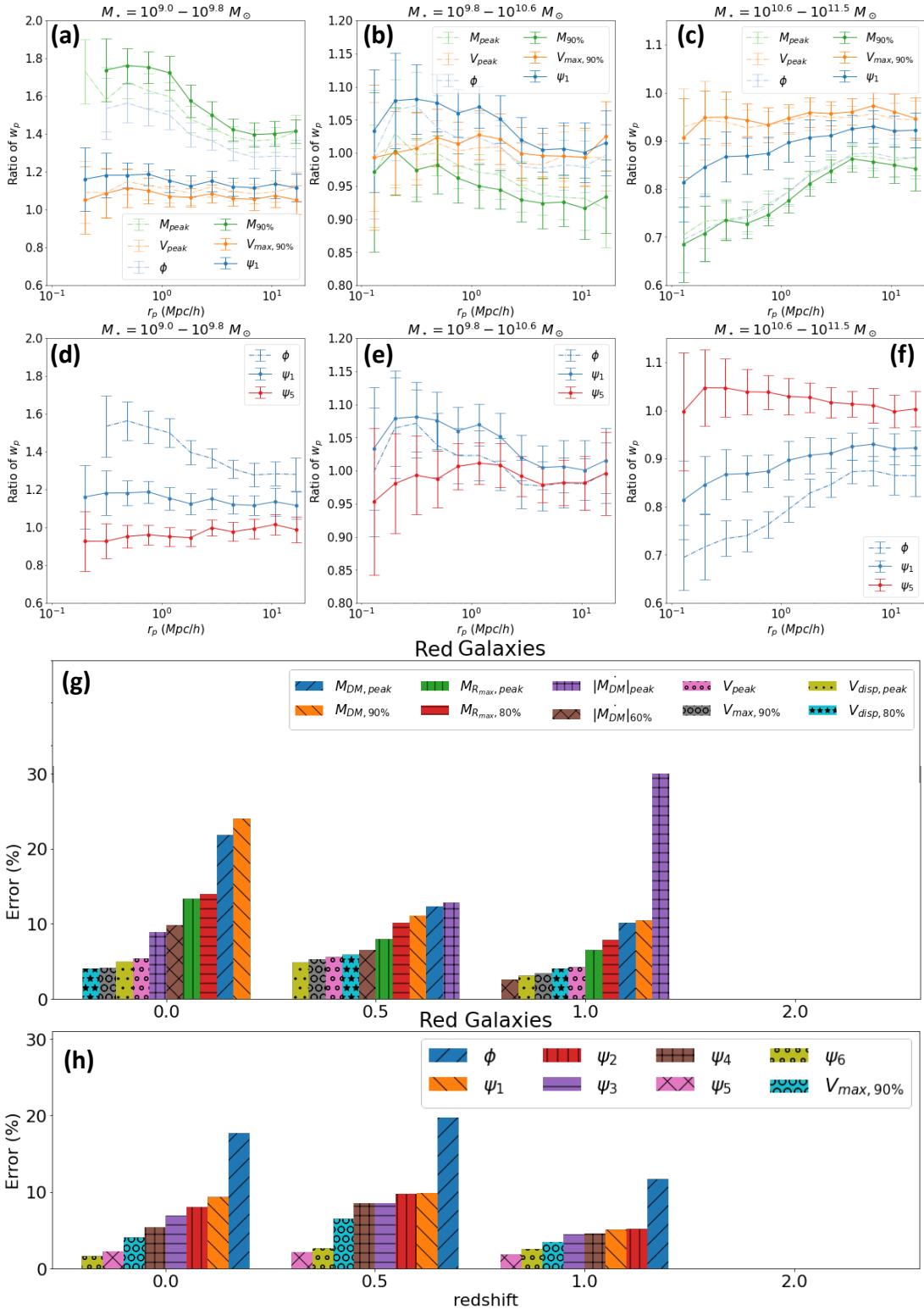


**Figure 3.** Same as Figure 2, but for red galaxies. There are not enough number of galaxy pairs at  $z = 2$  for reliable error estimation, forcing us to skip the redshift bin.

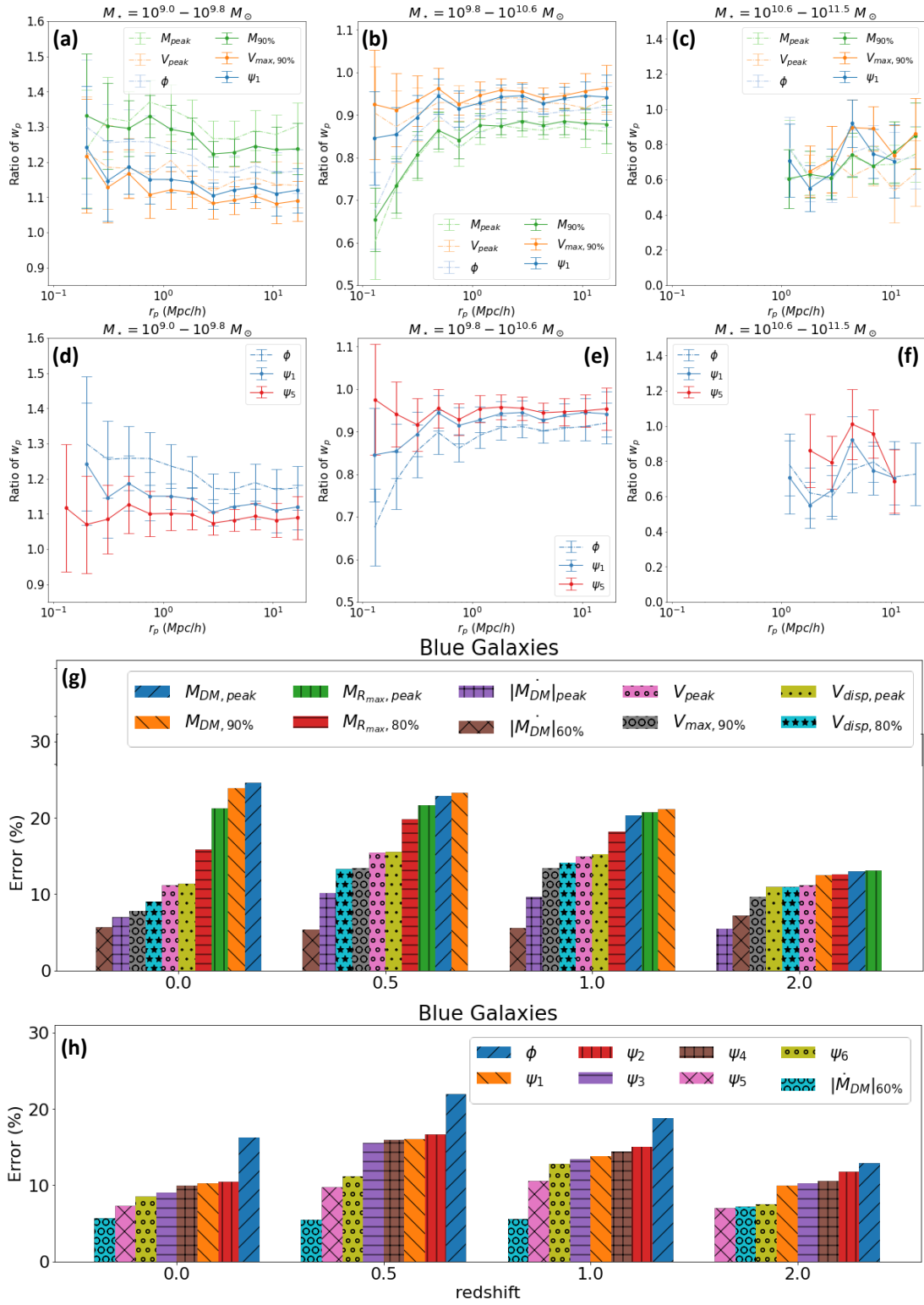


Figure 4. Same as Figure 2, but for blue galaxies.



directly ( $I_\sigma = (\sigma_{\text{peak}} - \sigma_{\text{perc}})/\sigma_{\text{peak}}$ , where  $\sigma_{\text{peak}}$  and  $\sigma_{\text{perc}}$  are the scatter with peak and percentiled quantities, respectively):

1.  $|\dot{M}_{DM}|$ :  $S = 1.843$ ,  $I_\sigma = 0.542$
2.  $V_{\text{disp}}$ :  $S = 1.419$ ,  $I_\sigma = 0.236$
3.  $V_{\text{max}}$ :  $S = 1.509$ ,  $I_\sigma = 0.153$
4.  $M_{R_{\text{max}}}$ :  $S = 1.487$ ,  $I_\sigma = 0.12$
5.  $M_{DM}$ :  $S = 1.283$ ,  $I_\sigma = 0.01$

The stochasticities are overall positively correlated with the improvements of switching from peak to percentiled quantities. We can see that the properties with maximal ( $|\dot{M}_{DM}|$ ) and minimal ( $M_{DM}$ ) stochasticity correspond to the largest and least relative improvements, respectively. A higher time resolution of the simulation might affect the best-fit percentiles of various properties considered here, especially for those with high stochasticities. However, due to the limitation of TNG300 time resolution, we are not able to further confirm this scenario.

In the usual implementation of SHAM with  $V_{\text{peak}}$ , a stellar mass function is used to assign  $M_\star$  to subhalos of the same number density. In so doing, a scatter between  $V_{\text{peak}}$  and  $M_\star$  is found to be necessary. In this work, we assign model galaxies to subhalos strictly follow the rank order, which effectively has introduced some scatter in our SHAM modeling.

One caveat for the success of the color dependence of clustering is that we have separated red subhalos from blue ones *a priori*, based on the full hydrodynamical run of TNG300, making our approach non-applicable to other dark matter only simulations.<sup>5</sup> In a companion paper (C.-Y. Chuang et al. 2022, in prep.), we have used a Graph Neural Network (GNN, e.g. Jespersen et al. 2022) model to emulate the TNG300 results, which enables one to “port” the TNG hydrodynamical model to any N-body simulations of similar resolutions as TNG300. Of course, with the GNN model, one then does not really require SHAM anymore, as our GNN model provides accurate predictions for  $M_\star$ ,  $g - r$  color, star formation rate, and several other properties, for galaxies with  $M_\star \geq 10^9 M_\odot$  at  $z = 0 - 2$ .

## 6. CONCLUSION

In recent years, the conditional abundance matching (Hearin et al. 2014; see also Masaki et al. 2013) approach has been used to exploit secondary connections

between galaxy and halo properties, which allows one to assign colors to model galaxies (e.g., Hearin et al. 2017). However, such models may not be compatible with the observed color-dependence of the central galaxy stellar mass–halo mass relation (SHMR; e.g., Mandelbaum et al. 2016). As our model is calibrated against TNG300, it can only reproduce the observed galaxy properties to the extent that TNG300 model does. It is found that, while the SHMR (irrespective of galaxy color) in TNG300 agrees with the measurements of Leauthaud et al. (2012), when central galaxies are split by color, only the red galaxy SHMR is reproduced. Finally, we note that there may well be an intrinsic scatter for the  $M_\star$  prediction through SHAM in the real universe, while the scatter associated with the “best” SHAM scheme could be smaller than the intrinsic scatter. Thus, our  $\psi_5$ -based SHAM scheme may inherit potential biases created by the numerical simulation we rely on.

Therefore, for a more realistic (and useful) application of the methodology developed in this work, in a future paper, we plan to tune our  $\psi$ ’s by directly fitting to observations, such as the clustering measurements from Sloan Digital Sky Survey and its subsequent surveys, as well as deeper surveys like DEEP2, PRIMUS, VIPERS, UltraVISTA (e.g., Coil et al. 2008; Zehavi et al. 2011; Guo et al. 2014; Marulli et al. 2013; Skibba et al. 2014; McCracken et al. 2015; Coil et al. 2017).

1 We thank Shogo Masaki, Yao-Yuan Mao, Chris-  
2 tian Jespersen, and Hong Guo for helpful com-  
3 ments. The numerical work was conducted on the  
4 high-performance computing facility at the Institute  
5 of Astronomy and Astrophysics in Academia Sinica  
6 (<https://hpc.tiara.sinica.edu.tw>) We acknowledge sup-  
7 ports from the National Science and Technology Council  
8 of Taiwan under grants MOST 110-2112-M-001-004 and  
9 MOST 109-2112-M-001-005. YTL thanks IH, LYL and  
10 ALL for constant encouragement and inspiration.

<sup>5</sup> Please note that our  $\psi_5$  can still accurately predict the stellar mass dependence of 2PCFs at  $z = 0 - 2$ .

**Table 1.** Scatter and loss of stellar mass prediction via different abundance matching scheme. The best values are bold faced and color shaded.

Loss Metrics		Stellar Mass Prediction								Prediction of $w_p$				Prediction of $w_p$					
Galaxy Types		All		Central		Satellite		Mix		All	Red	Blue	All	Mix	Red	Blue			
AM Scheme		Scatter	Loss	Scatter	Loss	Scatter	Loss	Scatter	Loss	Percentage Error				Percentage Error					
redshift 0		redshift 1.0														redshift 2.0			
$M_{DM,peak}$		0.195	0.148	0.176	0.133	0.194	0.148	0.180	0.136	26.3 ± 3.5	21.8 ± 5.0	24.6 ± 5.5	0.2096	0.1945	0.2144	0.1981	19.8 ± 4.1	9.4 ± 11.0	20.7 ± 5.2
$M_{DM,90\%}$		0.193	0.146	0.169	0.127	0.192	0.147	0.175	0.132	27.5 ± 3.4	24.0 ± 4.9	23.9 ± 5.2	0.2032	0.1866	0.2089	0.1907	19.5 ± 4.1	10.9 ± 10.2	21.0 ± 5.3
$M_{R_{max},peak}$		0.249	0.191	0.244	0.187	0.241	0.184	0.244	0.186	19.4 ± 3.4	13.3 ± 4.8	21.2 ± 5.6	0.2607	0.2528	0.2566	0.2535	19.6 ± 4.5	7.1 ± 10.6	21.4 ± 5.6
$M_{R_{max},80\%}$		0.219	0.166	0.211	0.160	0.217	0.165	0.213	0.162	18.2 ± 3.5	13.9 ± 4.9	15.9 ± 4.5	0.2428	0.2356	0.2436	0.2370	16.7 ± 4.4	7.8 ± 11.2	18.0 ± 5.3
$ M_{DM} _{peak}$		0.432	0.350	0.439	0.355	0.406	0.329	0.431	0.349	08.2 ± 3.6	8.9 ± 04.6	7.0 ± 5.1	0.4189	0.4206	0.4056	0.4180	8.0 ± 4.3	27.2 ± 11.0	10.0 ± 5.1
$ M_{DM} _{60\%}$		0.198	0.152	0.192	0.146	0.199	0.153	0.194	0.148	7.6 ± 3.7	9.8 ± 4.6	5.7 ± 4.5	0.1989	0.1983	0.1998	0.1985	5.0 ± 4.4	7.7 ± 12.4	6.1 ± 5.8
$V_{peak}$		0.177	0.136	0.174	0.134	0.180	0.139	0.175	0.135	8.5 ± 3.6	5.4 ± 4.5	11.2 ± 4.6	0.1783	0.1744	0.1765	0.1748	13.6 ± 4.2	7.1 ± 11.8	15.9 ± 5.5
$V_{max,90\%}$		0.150	0.115	0.147	0.112	0.156	0.120	0.149	0.114	5.8 ± 3.6	4.1 ± 4.6	7.8 ± 4.6	0.1558	0.1525	0.1536	0.1527	11.2 ± 4.3	7.7 ± 11.2	13.5 ± 5.6
$V_{disp,peak}$		0.191	0.148	0.188	0.145	0.196	0.153	0.190	0.147	8.3 ± 3.5	4.9 ± 4.6	11.4 ± 4.6	0.2007	0.1972	0.2001	0.1977	13.7 ± 4.2	5.2 ± 10.9	15.7 ± 5.5
$V_{disp,80\%}$		0.146	0.112	0.144	0.111	0.150	0.115	0.146	0.112	5.8 ± 3.6	4.1 ± 4.7	9.1 ± 4.8	0.1663	0.1648	0.1586	0.1638	12.2 ± 4.3	8.9 ± 10.7	14.4 ± 5.5
$\phi$		0.1667	0.1266	0.1449	0.1096	0.1790	0.1393	0.1533	0.1164	19.8 ± 3.6	17.7 ± 4.9	16.3 ± 5.1	0.1800	0.1613	0.1958	0.1678	18.5 ± 4.3	11.3 ± 9.9	19.6 ± 5.3
$\psi_1$		0.1458	0.1112	0.1400	0.1063	0.1497	0.1147	0.1423	0.1082	9.6 ± 3.5	9.4 ± 4.8	10.2 ± 4.4	0.1572	0.1529	0.1544	0.1531	12.5 ± 4.2	10.2 ± 10.9	14.9 ± 5.6
$\psi_2$		0.1436	0.1099	0.1405	0.1073	0.1460	0.1121	0.1418	0.1084	9.1 ± 3.6	8.1 ± 4.7	10.5 ± 4.8	0.1652	0.1624	0.1589	0.1618	13.6 ± 4.5	8.6 ± 9.5	15.7 ± 5.8
$\psi_3$		0.1457	0.1109	0.1419	0.1077	0.1500	0.1145	0.1438	0.1093	7.8 ± 3.6	6.9 ± 4.7	9.0 ± 4.5	0.1595	0.1558	0.1563	0.1559	11.6 ± 4.4	8.4 ± 9.9	13.7 ± 5.6
$\psi_4$		0.1445	0.1104	0.1425	0.1087	0.1470	0.1127	0.1435	0.1096	7.3 ± 3.7	5.4 ± 4.5	9.9 ± 4.6	0.1702	0.1683	0.1619	0.1672	12.7 ± 4.4	10.3 ± 11.2	14.7 ± 5.5
$\psi_5$		0.1415	0.1083	0.1391	0.1064	0.1470	0.1134	0.1410	0.1080	3.8 ± 3.7	2.3 ± 4.3	7.3 ± 4.7	0.1511	0.1501	0.1484	0.1498	8.9 ± 4.3	5.2 ± 10.8	10.3 ± 5.5
$\psi_6$		0.1427	0.1095	0.1412	0.1082	0.1463	0.1128	0.1424	0.1092	4.5 ± 3.4	1.7 ± 4.5	8.5 ± 4.8	0.1603	0.1602	0.1553	0.1594	10.9 ± 4.1	5.1 ± 10.9	12.9 ± 5.5
$M_{DM,peak}$		0.2053	0.1565	0.1869	0.1425	0.2082	0.1592	0.1915	0.1459	23.4 ± 3.8	17.1 ± 8.4	23.7 ± 5.7	0.2196	0.2093	0.2268	0.2116	11.7 ± 4.7	9.3 ± 8.7	12.7 ± 5.3
$M_{DM,90\%}$		0.2003	0.1512	0.1795	0.1347	0.2027	0.1558	0.1845	0.1391	23.6 ± 3.9	18.3 ± 7.8	24.8 ± 5.6	0.2066	0.1968	0.2171	0.1995	12.1 ± 4.7	3.5 ± 7.8	12.9 ± 5.4
$M_{R_{max},peak}$		0.2601	0.2005	0.2521	0.1945	0.2545	0.1955	0.2526	0.1947	20.7 ± 3.8	14.5 ± 8.7	22.8 ± 5.8	0.2631	0.2570	0.2612	0.2575	12.1 ± 4.9	2.6 ± 8.1	12.8 ± 5.5
$M_{R_{max},80\%}$		0.2354	0.1791	0.2272	0.1723	0.2350	0.1797	0.2288	0.1739	18.5 ± 3.8	15.9 ± 8.8	20.5 ± 5.5	0.2515	0.2485	0.2500	0.2487	11.4 ± 5.1	3.2 ± 7.1	12.8 ± 5.6
$ M_{DM} _{peak}$		0.4296	0.3463	0.4328	0.3485	0.4123	0.3345	0.4287	0.3456	9.2 ± 3.7	12.8 ± 7.9	10.7 ± 5.3	0.4002	0.4010	0.3903	0.3997	4.9 ± 4.8	28.4 ± 8.5	6.5 ± 5.3
$ M_{DM} _{60\%}$		0.1949	0.1487	0.1926	0.1464	0.1969	0.1513	0.1935	0.1474	6.0 ± 3.8	8.7 ± 8.0	5.4 ± 5.3	0.2213	0.2220	0.2156	0.2212	6.4 ± 5.3	1.1 ± 5.9	6.9 ± 5.9
$V_{peak}$		0.1765	0.1358	0.1725	0.1327	0.1767	0.1364	0.1734	0.1334	12.4 ± 3.8	7.8 ± 8.6	16.3 ± 6.1	0.1948	0.1924	0.1874	0.1918	9.8 ± 5.2	1.3 ± 5.4	11.0 ± 5.9
$V_{max,90\%}$		0.1508	0.1135	0.1471	0.1101	0.1524	0.1163	0.1482	0.1114	10.4 ± 3.8	6.5 ± 8.5	15.1 ± 5.9	0.1757	0.1742	0.1657	0.1732	8.8 ± 5.3	1.5 ± 7.3	9.9 ± 5.9
$V_{disp,peak}$		0.1953	0.1509	0.1913	0.1477	0.1974	0.1526	0.1926	0.1487	12.3 ± 4.0	6.4 ± 8.2	16.1 ± 6.0	0.2205	0.2184	0.2156	0.2180	9.5 ± 5.2	1.6 ± 7.6	10.3 ± 5.8
$V_{disp,80\%}$		0.1551	0.1171	0.1533	0.1152	0.1523	0.1162	0.1531	0.1154	11.0 ± 3.6	6.9 ± 8.3	15.1 ± 6.2	0.1911	0.1911	0.1766	0.1893	10.2 ± 5.3	2.1 ± 7.0	11.7 ± 5.7
$\phi$		0.1748	0.1308	0.1520	0.1147	0.1916	0.1480	0.1609	0.1215	20.4 ± 3.8	19.8 ± 8.2	21.9 ± 5.8	0.2014	0.1917	0.1956	0.1922	11.7 ± 5.6	9.4 ± 9.5	13.1 ± 6.2
$\psi_1$		0.1507	0.1134	0.1459	0.1089	0.1513	0.1154	0.1470	0.1102	11.7 ± 3.9	9.9 ± 9.0	16.0 ± 5.8	0.1761	0.1740	0.1671	0.1731	8.7 ± 5.7	1.5 ± 6.2	9.7 ± 6.4
$\psi_2$		0.1549	0.1170	0.1519	0.1140	0.1518	0.1158	0.1519	0.1144	12.4 ± 3.8	9.8 ± 8.4	16.7 ± 6.0	0.1816	0.1784	0.1761	0.1781	10.4 ± 5.6	2.1 ± 6.6	11.6 ± 6.0
$\psi_3$		0.1511	0.1137	0.1471	0.1099	0.1517	0.1155	0.1481	0.1111	11.2 ± 3.8	8.6 ± 8.1	15.5 ± 5.7	0.1786	0.1767	0.1698	0.1759	9.7 ± 5.1	2.0 ± 6.5	10.8 ± 5.7
$\psi_4$		0.1568	0.1182	0.1547	0.1160	0.1529	0.1165	0.1544	0.1161	11.7 ± 3.7	8.6 ± 8.9	15.9 ± 6.0	0.1942	0.1939	0.1802	0.1923	9.9 ± 5.0	1.9 ± 6.9	11.3 ± 5.3
$\psi_5$		0.1449	0.1093	0.1438	0.1081	0.1461	0.1118	0.1443	0.1088	7.3 ± 3.8	2.2 ± 8.0	9.8 ± 6.1	0.1697	0.1694	0.1609	0.1684	6.6 ± 5.3	1.1 ± 7.4	7.4 ± 5.7
$\psi_6$		0.1510	0.1141	0.1505	0.1134	0.1496	0.1146	0.1504	0.1137	8.5 ± 3.9	2.6 ± 8.0	11.2 ± 6.4	0.1800	0.1804	0.1713	0.1793	6.9 ± 5.4	1.1 ± 6.1	7.6 ± 6.0

## REFERENCES

- Coil, A. L., Mendez, A. J., Eisenstein, D. J., & Moustakas, J. 2017, *ApJ*, 838, 87, doi: [10.3847/1538-4357/aa63ec](https://doi.org/10.3847/1538-4357/aa63ec)
- Coil, A. L., Newman, J. A., Croton, D., et al. 2008, *ApJ*, 672, 153, doi: [10.1086/523639](https://doi.org/10.1086/523639)
- Conroy, C., Wechsler, R. H., & Kravtsov, A. V. 2006, *ApJ*, 647, 201, doi: [10.1086/503602](https://doi.org/10.1086/503602)
- Guo, H., Zheng, Z., Zehavi, I., et al. 2014, *MNRAS*, 441, 2398, doi: [10.1093/mnras/stu763](https://doi.org/10.1093/mnras/stu763)
- Hearin, A. P., Watson, D. F., Becker, M. R., et al. 2014, *MNRAS*, 444, 729, doi: [10.1093/mnras/stu1443](https://doi.org/10.1093/mnras/stu1443)
- Hearin, A. P., Campbell, D., Tollerud, E., et al. 2017, *AJ*, 154, 190, doi: [10.3847/1538-3881/aa859f](https://doi.org/10.3847/1538-3881/aa859f)
- Jespersen, C. K., Cranmer, M., Melchior, P., et al. 2022, **Mangrove**: Learning Galaxy Properties from Merger Trees, arXiv, doi: [10.48550/ARXIV.2210.13473](https://doi.org/10.48550/ARXIV.2210.13473)
- Kravtsov, A. V., Berlind, A. A., Wechsler, R. H., et al. 2004, *ApJ*, 609, 35
- Leauthaud, A., Tinker, J., Bundy, K., et al. 2012, *ApJ*, 744, 159, doi: [10.1088/0004-637X/744/2/159](https://doi.org/10.1088/0004-637X/744/2/159)
- Lehmann, B. V., Mao, Y.-Y., Becker, M. R., Skillman, S. W., & Wechsler, R. H. 2017, *ApJ*, 834, 37, doi: [10.3847/1538-4357/834/1/37](https://doi.org/10.3847/1538-4357/834/1/37)
- Lin, Y.-T., Mandelbaum, R., Huang, Y.-H., et al. 2016, *ApJ*, 819, 119, doi: [10.3847/0004-637X/819/2/119](https://doi.org/10.3847/0004-637X/819/2/119)
- Lin, Y.-T., Miyatake, H., Guo, H., et al. 2022, *A&A*, 666, A97, doi: [10.1051/0004-6361/202244404](https://doi.org/10.1051/0004-6361/202244404)
- Mandelbaum, R., Wang, W., Zu, Y., et al. 2016, *MNRAS*, 457, 3200, doi: [10.1093/mnras/stw188](https://doi.org/10.1093/mnras/stw188)
- Marulli, F., Bolzonella, M., Branchini, E., et al. 2013, *A&A*, 557, A17, doi: [10.1051/0004-6361/201321476](https://doi.org/10.1051/0004-6361/201321476)
- Masaki, S., Kashino, D., & Lin, Y.-T. 2022, arXiv e-prints, arXiv:2210.11713. <https://arxiv.org/abs/2210.11713>
- Masaki, S., Lin, Y.-T., & Yoshida, N. 2013, *MNRAS*, 436, 2286, doi: [10.1093/mnras/stt1729](https://doi.org/10.1093/mnras/stt1729)
- McCracken, H. J., Wolk, M., Colombi, S., et al. 2015, *MNRAS*, 449, 901, doi: [10.1093/mnras/stv305](https://doi.org/10.1093/mnras/stv305)
- Nelson, D., Pillepich, A., Springel, V., et al. 2018, *MNRAS*, 475, 624, doi: [10.1093/mnras/stx3040](https://doi.org/10.1093/mnras/stx3040)
- Pillepich, A., Nelson, D., Hernquist, L., et al. 2018, *MNRAS*, 475, 648, doi: [10.1093/mnras/stx3112](https://doi.org/10.1093/mnras/stx3112)
- Reddick, R. M., Wechsler, R. H., Tinker, J. L., & Behroozi, P. S. 2013, *ApJ*, 771, 30, doi: [10.1088/0004-637X/771/1/30](https://doi.org/10.1088/0004-637X/771/1/30)
- Sinha, M., & Garrison, L. 2019, in *Software Challenges to Exascale Computing*, ed. A. Majumdar & R. Arora (Singapore: Springer Singapore), 3–20. [https://doi.org/10.1007/978-981-13-7729-7\\_1](https://doi.org/10.1007/978-981-13-7729-7_1)
- Sinha, M., & Garrison, L. H. 2020, *MNRAS*, 491, 3022, doi: [10.1093/mnras/stz3157](https://doi.org/10.1093/mnras/stz3157)
- Skibba, R. A., Smith, M. S. M., Coil, A. L., et al. 2014, *ApJ*, 784, 128, doi: [10.1088/0004-637X/784/2/128](https://doi.org/10.1088/0004-637X/784/2/128)
- Springel, V., White, S. D. M., Tormen, G., & Kauffmann, G. 2001, *MNRAS*, 328, 726, doi: [10.1046/j.1365-8711.2001.04912.x](https://doi.org/10.1046/j.1365-8711.2001.04912.x)
- Springel, V., Pakmor, R., Pillepich, A., et al. 2018, *MNRAS*, 475, 676, doi: [10.1093/mnras/stx3304](https://doi.org/10.1093/mnras/stx3304)
- Tasitsiomi, A., Kravtsov, A. V., Wechsler, R. H., & Primack, J. R. 2004, *ApJ*, 614, 533, doi: [10.1086/423784](https://doi.org/10.1086/423784)
- Tonnesen, S., & Ostriker, J. P. 2021, *ApJ*, 917, 66, doi: [10.3847/1538-4357/ac0724](https://doi.org/10.3847/1538-4357/ac0724)
- Vale, A., & Ostriker, J. P. 2004, *MNRAS*, 353, 189, doi: [10.1111/j.1365-2966.2004.08059.x](https://doi.org/10.1111/j.1365-2966.2004.08059.x)
- Wechsler, R. H., & Tinker, J. L. 2018, *ARA&A*, 56, 435, doi: [10.1146/annurev-astro-081817-051756](https://doi.org/10.1146/annurev-astro-081817-051756)
- Zehavi, I., Zheng, Z., Weinberg, D. H., et al. 2011, *ApJ*, 736, 59, doi: [10.1088/0004-637X/736/1/59](https://doi.org/10.1088/0004-637X/736/1/59)
- Zentner, A. R., Hearin, A. P., & van den Bosch, F. C. 2014, *MNRAS*, 443, 3044, doi: [10.1093/mnras/stu1383](https://doi.org/10.1093/mnras/stu1383)